

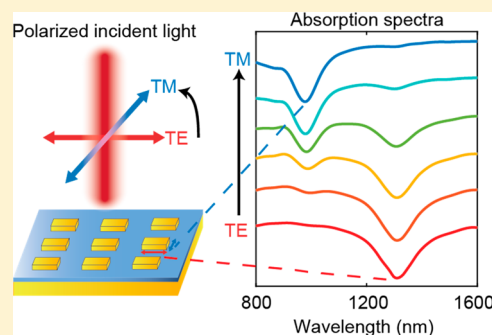
Polarization-Controlled Nanogap Cavity with Dual-Band and Spatially Overlapped Resonances

Qixin Shen,^{†,⊥} Andrew M. Boyce,^{‡,⊥} Guoce Yang,^{‡,§,⊥} and Maiken H. Mikkelsen^{*,†,‡,⊥}[†]Department of Physics, Duke University, Durham, North Carolina 27708, United States[‡]Department of Electrical and Computer Engineering, Duke University, Durham, North Carolina 27708, United States[§]State Key Laboratory of Precision Measurement Technology and Instruments, Department of Precision Instrument, Tsinghua University, Beijing 100084, China

S Supporting Information

ABSTRACT: Metasurfaces are ultrathin, two-dimensional arrays of sub-wavelength resonators, which can possess optical properties unobtainable naturally. One such desirable property is dual-band absorption occurring at the same spatial location, which could enable the enhancement of multiple processes simultaneously. However, demonstrations of multiband absorption to date have been limited to the mid-infrared and microwave regimes. Here, metasurfaces are demonstrated to have spatially overlapped, dual-band absorption in the visible to near-infrared using arrays of plasmonic nanogap cavities that consist of a sub-10 nm dielectric layer sandwiched between gold rectangles and a gold film. The relative strength of the two modes is tuned dynamically by varying the incident polarization, and the period between elements is used to tune the spectral bandwidth. Additionally, these near-perfect absorber structures fabricated by electron beam lithography (EBL) are compared to similar nanogap geometries fabricated using colloiddally synthesized nanoparticles. This comparison reveals that EBL nanogap structures can achieve similar absorption performance to colloidal nanoparticles while enabling a much greater control of the nanoparticle shape, size, and relative position. These widely tunable, dual-band metasurfaces may find applications in spectrally multiplexed photodetectors and for enhancement of optical processes, such as nonlinear generation and Stokes-shifted absorption and emission processes.

KEYWORDS: plasmonics, electron beam lithography, nanocube, metasurface, dual-band absorption



Light absorption is critical for many key applications including solar energy, optical communication, photocatalysis, and sensing. Engineered structures known as metasurfaces can be designed to strongly enhance light absorption^{1–9} and thus increase the efficiency of such optoelectronic devices.^{10–15} However, more advanced applications including multiplexed sensors and detectors and tailored optical processes at multiple wavelengths^{16–18} can be enabled by metasurfaces with two or more independently tunable absorption resonances. Dual-band absorption has been previously shown using pairs of metal–dielectric stacks¹⁹ and Jerusalem crosses in the mid-IR,²⁰ as well as in the GHz regime using a bullseye structure.²¹ Thermal emission has been controlled at multiple wavelengths using dual-band absorbers consisting of arrays of different sized crosses.²² Additionally, adjacent nanorods with different dimensions have been utilized to simultaneously detect multiple surface-enhanced infrared absorption signals,²³ and the use of biresonant photonic crystal cavities has been proposed for single small gas molecule detection using mid-IR photothermal spectroscopy.²⁴ However, despite appealing potential applications such as dual-band sensing, enhancement of embedded emitters, and nonlinear frequency conversion, structures with multiple spectrally tunable, spatially overlapped resonances in the visible and

near-infrared have been largely unexplored. Biresonant structures would offer the unique advantage of simultaneous large enhancement of both the excitation and emission rates of embedded emitters, potentially leading to significantly greater overall enhancement in the fluorescence and the development of brighter LEDs and transmitters for optical communication applications. Nonlinear optical processes could also greatly benefit from use of dual-band resonances. For example, spontaneous parametric down-conversion has a very low intrinsic efficiency, and several orders of magnitude of enhancement is necessary for significant generation at the nanoscale to enable on-chip creation of entangled photon pairs for quantum information processing, particularly at telecom wavelengths. The near-IR band is also promising for nonlinear frequency conversion for applications such as bioimaging, drug delivery, and photovoltaics.

Here we show that arrays of nanorectangles fabricated by electron beam lithography (EBL) and separated from a gold ground plane by a sub-10 nm dielectric layer display two absorption resonances in the near-infrared which can be

Received: June 11, 2019

Published: July 3, 2019

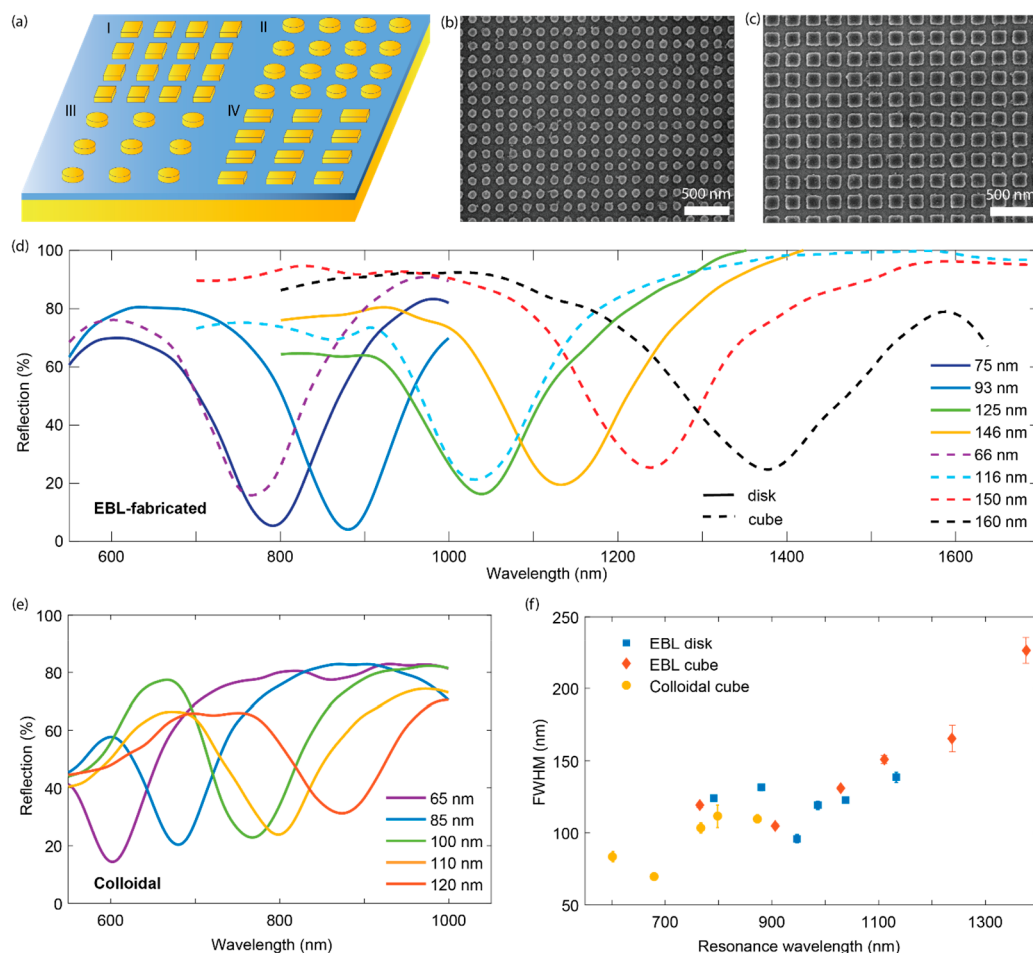


Figure 1. (a) Structure of the sample: patterned gold elements (height 30 nm) separated from a gold ground plane by 7 nm of Al₂O₃. The sample has four distinct sections: (I) cubes of different sizes with a fixed fill fraction of ~25%; (II) disks of different sizes with a fixed fill fraction of ~25%; (III) disks with various fill fractions; (IV) rectangles with various ratios of width and length. Nine, 12, or 16 elements are shown for clarity; however, the actual size of one array is 100 $\mu\text{m} \times 100 \mu\text{m}$ and contains over 10 000 elements. (b) SEM images of 93 nm EBL-fabricated disks. (c) SEM images of 160 nm EBL-fabricated cubes (scale bar is 500 nm). (d) Reflection spectra of EBL-fabricated cubes and disks of various sizes. (e) Reflection spectra of colloidal synthesized silver nanocubes of different sizes. (f) Comparison of the full-width at half-maximum (fwhm) between EBL-fabricated disks, cubes, and colloidal silver nanocubes.

independently tuned and separated by as much as 500 nm. Furthermore, finite-element simulations (COMSOL Multiphysics) confirm the spatial overlap of these two modes, which is critical for leveraging both modes simultaneously. The geometry of the sample consists of precisely arranged ensembles of absorbing elements on a gold substrate separated by a thin dielectric layer (7 nm of Al₂O₃), shown in Figure 1a–c. This structure results in a waveguide cavity mode, giving rise to a resonance. The resonant wavelength is determined by the length and effective index of the waveguide cavity and, in this case, is controlled via the size of the patterned gold structures and the thickness of the Al₂O₃ layer. The charge distribution in the fundamental mode results in a current loop between the gold structures and gold substrate, thus inducing a strongly enhanced magnetic field. This enables the surface to be impedance matched to free space, resulting in near-perfect absorption of light.^{25–27} Four different types of EBL-fabricated nanoparticle arrays are investigated in this work: cubes of different sizes, disks of different sizes, disks with various fill fractions, and rectangles with different ratios of width and length. First, we study structures with a single fundamental resonance, including disks and cubes fabricated using both

EBL and colloidal synthesis, before examining dual-band rectangular absorbers.

To evaluate the performance of EBL-fabricated nanogap absorbers, reflection spectra were measured from film-coupled gold disks and cubes using a white light source at nearly normal incidence, as shown in Figure 1d (additional spectra in SI Figure 1). The resonance wavelength is tuned from the visible to the near-infrared by varying the size of the absorbing elements, thus changing the volume of the cavity. With a surface coverage density of approximately 25%, an absorption of 80% or greater can be achieved on resonance for eight different sizes. EBL-fabricated disks are observed to have higher peak absorption compared to EBL-fabricated cubes.

Previous literature shows that metasurfaces based on colloidal nanocubes show near-perfect absorption with a similar nanogap structure.^{25,27} However, to this point, it remained unclear whether similar performance could be obtained with EBL-fabricated nanoparticles, which are not limited by the variety of sizes and shapes that can be synthesized. To compare the performance of the EBL-fabricated film-coupled nanoparticles with colloidal nanoparticles, metasurfaces of colloidal silver nanocubes were

produced using a similar 7 nm Al_2O_3 layer on a gold ground plane (additional fabrication details in the SI). Figure 1e shows reflection spectra of these metasurfaces for nanocubes with side lengths from 65 to 120 nm. In these experiments, for the same resonance wavelength, EBL-fabricated nanoparticles typically have higher peak absorption than colloidal nanocubes, which is most likely due to higher fill fractions and better size uniformity. In addition, the full-widths at half-maximum (fwhm) are extracted from the spectra for both the colloidal nanocubes and the EBL-fabricated particles and are shown as a function of resonance wavelength in Figure 1f. The bandwidth of EBL-fabricated and colloidal samples is comparable at similar resonance wavelengths, demonstrating that the resultant plasmonic cavities have similar quality factors.

To control the peak absorption and the width of the plasmon resonance, critical to, for example, photovoltaics²⁸ and photoluminescence enhancement,^{29,30} arrays of 100 nm disks were fabricated with different periods and, thus, different fill fractions of absorbing elements on the surface. The reflection spectra for each of these arrays are shown in Figure 2a, and the corresponding SEM images are shown in Figure 2b.

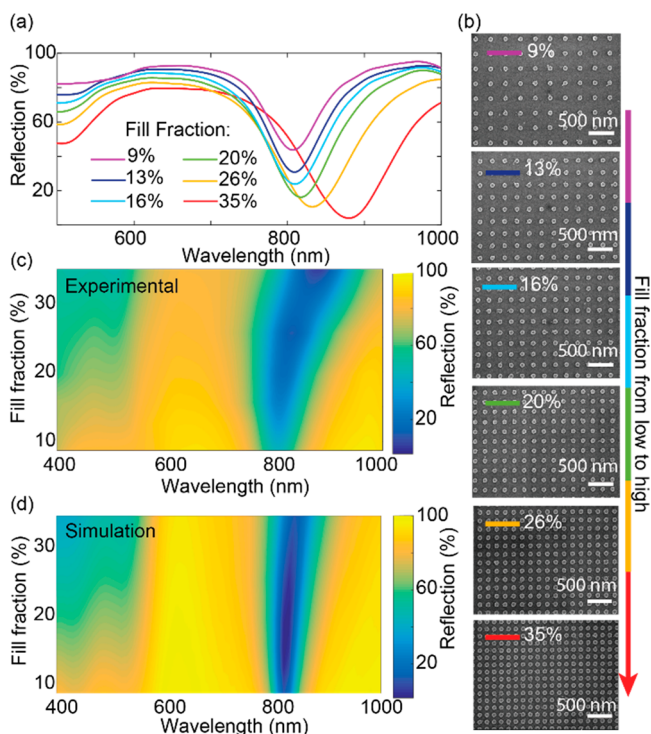


Figure 2. (a) Reflection spectra from disks with various fill fractions, which show that the fwhm of the spectra is sensitive to the density of gold disks. The fill fractions range from 9% to 35%. (b) SEM images of the disk arrays in (a) in order of increasing fill fraction. (c) Experimental contour plot of reflection spectra with variable fill fraction. For clarity, interpolation is used between data points. (d) Simulated reflection spectra using the same dimensions as (c) for comparison, showing good agreement with experiments.

It is seen that at higher fill fractions the fwhm of the plasmon resonance increases from 80 nm to 122 nm. Additionally, the resonance wavelength red-shifts with increasing fill fraction, in particular for the highest fill fraction of 35%. The simulations shown in Figure 2d are found to be consistent with experiments for fill fractions below 26%. However, at the highest fill fraction, a significant red-shift in the resonance

wavelength is observed experimentally, which may be explained by near-field coupling between neighboring elements delocalizing the plasmon mode.³¹

Next, to realize nanostructures with two resonances that can be tuned independently of each other, we investigate arrays of rectangular elements. By utilizing the two different dimensions in a single rectangle absorber, two resonances can be obtained simultaneously. Polarized light can be used to access either the transverse or longitudinal modes, which originate from the width and length of the rectangle, respectively. The transverse electric (TE) configuration occurs when the polarization of incident light is along the length, while the transverse magnetic (TM) configuration occurs when the polarization of incident light is along the width. As the polarization of the incident light varies from along the length dimension to along the width, the amount of coupling of the incident light into the two modes varies, resulting in a reduction in the amplitude of the longitudinal mode and an increase in the amplitude of the transverse mode, which reaches a maximum when the polarization is in the TM configuration. For the 110 nm width and 150 nm length rectangles, shown in Figure 3a, this

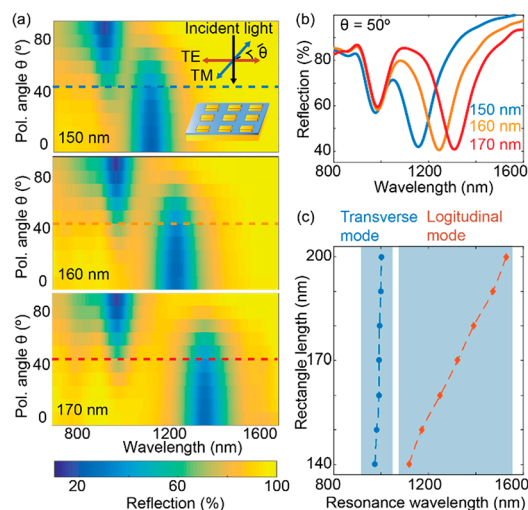


Figure 3. (a) Reflection spectra from rectangle absorbers with varying white light polarization angle from transverse electric (TE) configuration to transverse magnetic (TM) configuration. The width of rectangular absorbers is 110 nm, while the length ranges from 150 nm to 170 nm. The inset shows the TE configuration and TM configuration when white light is incident on the sample. (b) Reflection spectra from the rectangle absorbers shown in (a) when the incident white light polarization is 50° . (c) Resonance wavelength of rectangle absorbers as a function of rectangle length from 140 nm to 200 nm. The transverse mode associated with the 110 nm width dimension is at approximately 1000 nm, while the longitudinal mode can be tailored from 1118 nm to 1527 nm.

tuning corresponds to a gradual shift in the resonance wavelength from 982 nm to 1172 nm. Additionally, rectangles with 160 and 170 nm length were investigated to further examine tailored double resonances on a single element; their polarization-dependent absorption properties are also shown in Figure 3a. When the incident polarization is near 45° , there is significant absorption into both the TE and TM modes. This can be seen in the absorption spectra for the 150, 160, and 170 nm by 110 nm rectangles with 50° incident polarization shown in Figure 3b.

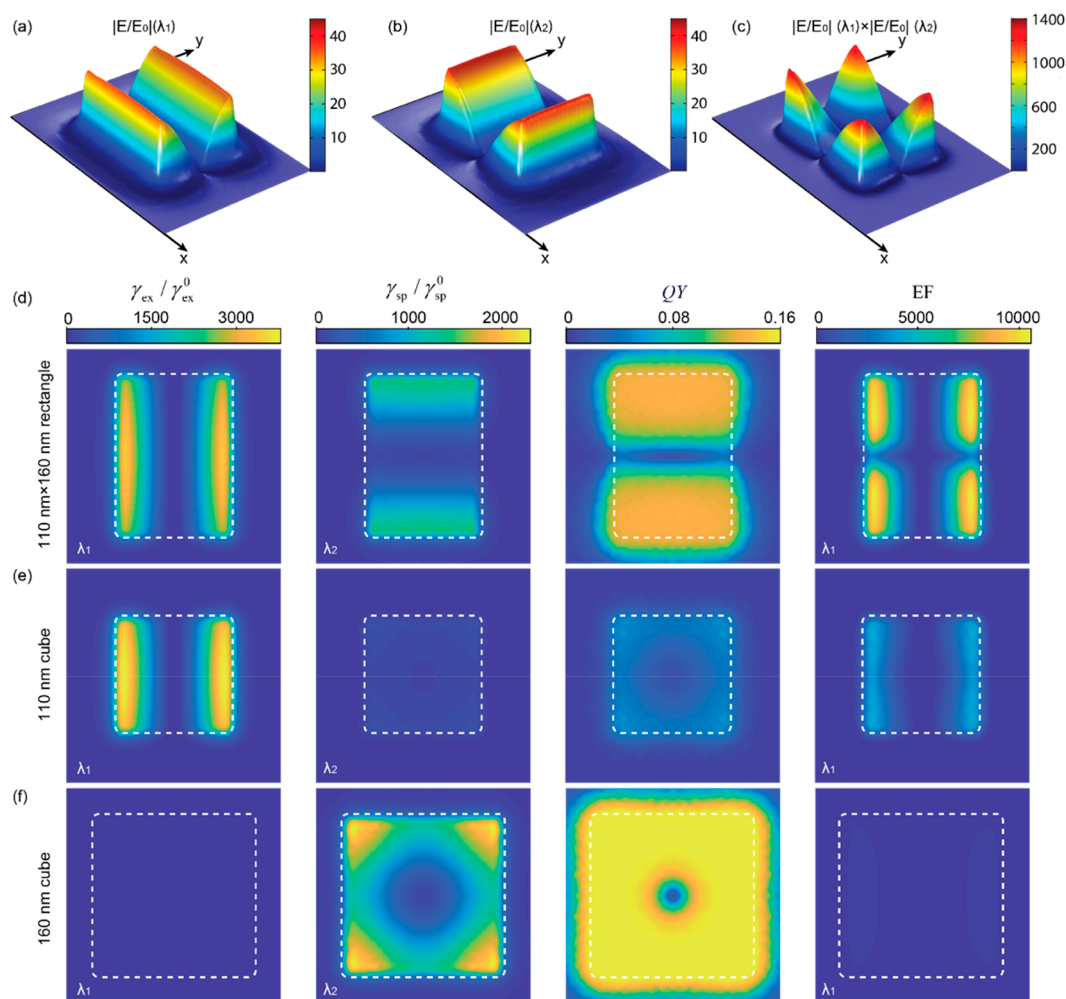


Figure 4. (a–c) Spatial distribution of electric field enhancement in the gap of a film coupled, 110×160 nm rectangular nanoantenna. (a) Transverse gap plasmon mode excited by TM-polarized light at a resonance wavelength of 990 nm. (b) Longitudinal gap plasmon mode excited by TE-polarized light at a resonance wavelength of 1250 nm. (c) The product of the electric field enhancements in (a) and (b); local maxima indicate regions where the two gap plasmon modes are strongly spatially overlapped. (d, e) Spatial distribution of excitation rate enhancement $\gamma_{ex}/\gamma_{ex}^0$, spontaneous emission rate enhancement $\gamma_{sp}/\gamma_{sp}^0$, quantum yield QY, and total fluorescence enhancement EF for (d) 110×160 nm nanorectangle, (e) 110 nm nanocube, and (f) 160 nm nanocube.

To highlight the independent tuning of the two resonances, seven different arrays of rectangles with fixed width and varying lengths were fabricated. Figure 3c shows the resonance wavelengths for the two absorption modes of each array, which were measured using an incident polarization of $\theta = 50^\circ$. A transverse resonance mode associated with the width dimension was observed at approximately 1000 nm in all cases, while the longitudinal resonance mode associated with the length varies from 1118 nm to 1527 nm. Thus, spectral separations between the transverse and longitudinal modes can be tuned from ~ 100 nm to more than 500 nm by varying the length of the rectangles. We note that the transverse mode at around 1000 nm has a slight red-shift with increasing length, even though the width design is fixed at 110 nm. This may be explained by the bleeding effect in the lithography process, which results in slightly larger widths than those chosen in the design as the length of the rectangles is increased, causing a red-shift in the resonance wavelength. Another potential contributing factor could be interactions between the transverse and longitudinal modes.

To demonstrate that the transverse and longitudinal modes in rectangular absorbing elements can be utilized simultaneously, the electric field distribution is calculated using full-wave simulations based on the finite-element method (COMSOL Multiphysics) at the resonance wavelengths of both the transverse and longitudinal modes for 110×160 nm rectangles. For the resonance wavelengths of both modes, the electric field shows large, over 45-fold, enhancement along the two sides of the rectangle that are perpendicular to the incident polarization. In addition to demonstrating two resonance modes with spectral separation controlled by the difference between the rectangle's width and length, we further show that the enhanced electric fields from these two resonance modes possess good spatial overlap. To further illustrate this spatial overlap, the spatial distribution of the field enhancement is shown in Figure 4c for 990 and 1250 nm light impinging on the nanorectangle, which matches the two resonance wavelengths. This spatial distribution is calculated by multiplying the field enhancements from Figure 4a and b. The field enhancements could be even greater by utilizing a thinner dielectric layer than the 7 nm of Al_2O_3 used in this work. The

enhanced electric field at two wavelengths with good spatial overlap are promising for optical processes involving multiple wavelengths. Fluorescent emission is selected as an example to illustrate the advantage of these dual resonances; however, other processes such as harmonic generation and four-wave mixing could also benefit. Specifically, it is assumed that a dipole emitter, such as a PbS quantum dot, with an emission wavelength of 1250 nm is placed in the nanogap and excited by 990 nm light with polarization perpendicular to the nanorectangle's width. It is shown in Figure 4d that the total fluorescence enhancement factor EF and spontaneous emission rate enhancement $\gamma_{sp}/\gamma_{sp}^0$ achieve large enhancements compared with an emitter placed on glass as a control. The simulated dependence of this enhancement on the emitter position is obtained by sequentially placing a single dipole emitter on a discrete 41×41 grid in the nanogap underneath the nanorectangle. The emission rate enhancement can be attributed to the increased local density of states due to the presence of the longitudinal mode centered at the emission wavelength, while the total fluorescence enhancement factor EF is a consequence of both the transverse and longitudinal modes, and defined as

$$EF = \frac{\eta\gamma_{ex}QY}{\eta^0\gamma_{ex}^0QY^0} \quad (1)$$

where η is the collection efficiency, γ_{ex} is the excitation rate, QY is the quantum yield, and the superscript "0" refers to the emitter on glass. The transverse mode at 990 nm causes the excitation rate enhancement distribution depicted, while the longitudinal mode at 1250 nm enhances the photon out-coupling channel and thus results in the spontaneous emission rate enhancement and quantum yield enhancement distributions shown. The final EF pattern can be regarded as the result of the spatial overlap of the two modes according to eq 1, similar to the product of the electric field distributions shown in Figure 4c. Thus, the total fluorescence intensity and spontaneous emission rate can be enhanced simultaneously with dual-band resonances in a single nanoparticle. In order to compare the performance to singly resonant nanoparticles, simulations are also performed using the same method for 110 and 160 nm nanocubes. In those cases, either the total fluorescence or the spontaneous emission rate obtains large enhancement depending on whether the resonance of the nanocube is overlapped with the excitation or the emission wavelength. However, simultaneous enhancement cannot be achieved without the presence of dual-band resonances.

In summary, we have demonstrated a metasurface with two, near-perfect absorption resonances that can be independently tuned relative to each other through a range of more than 500 nm. The polarization of the incoming light provides a knob to tune the relative strength of the two resonances dynamically as well as transition from two to a single resonance. These metasurfaces operate in the visible and near-IR and possess resonances that are spectrally separated while spatially overlapped, which could provide critical advantages for multiplexed sensors and detectors, as well as processes such as stimulated Raman scattering, entangled photon generation, and multiphoton absorption. A vertical plasmonic gap structure was utilized that supports a highly confined gap-plasmon mode and consists of metal nanoparticles on a sub-10 nm dielectric film with an underlying gold ground plane.³² The metal nanoparticles were fabricated using both colloidal

nanoparticles and EBL and displayed similar absorption performance. This shows the promise for combined bottom-up and top-down fabrication, as atomic layer deposition enables single-nanometer control of the critical vertical gap dimension, while EBL allows for a wide variety of sizes and shapes of nanoparticles as well as deterministic element placement. This platform also opens up possibilities to tailor the radiation pattern, mix different sizes and shapes of nanoparticles, and create integrated waveguides.

■ ASSOCIATED CONTENT

📄 Supporting Information

The Supporting Information is available free of charge on the ACS Publications website at DOI: 10.1021/acsp Photonics.9b00851.

Additional details on the fabrication process, as well as reflection spectra for additional sizes of nanocubes and nanodisks fabricated by EBL (PDF)

■ AUTHOR INFORMATION

Corresponding Author

*E-mail: m.mikkelsen@duke.edu. Phone: +1 (919) 660-0185.

ORCID

Guoce Yang: 0000-0002-6566-7776

Maiken H. Mikkelsen: 0000-0002-0487-7585

Author Contributions

[†]Q.S. and A.M.B. contributed equally to this work.

Notes

The authors declare no competing financial interest.

■ ACKNOWLEDGMENTS

This work was supported by the Office of Naval Research (award no. N00014-17-1-2589) and a Cottrell Scholar award from the Research Corporation for Science Advancement.

■ REFERENCES

- (1) Sturmberg, B. C.; Chong, T. K.; Choi, D.-Y.; White, T. P.; Botten, L. C.; Dossou, K. B.; Poulton, C. G.; Catchpole, K. R.; McPhedran, R. C.; de Sterke, C. M. Total absorption of visible light in ultrathin weakly absorbing semiconductor gratings. *Optica* **2016**, *3* (6), 556–562.
- (2) Teperik, T. V.; De Abajo, F. G.; Borisov, A.; Abdelsalam, M.; Bartlett, P.; Sugawara, Y.; Baumberg, J. Omnidirectional absorption in nanostructured metal surfaces. *Nat. Photonics* **2008**, *2* (5), 299–301.
- (3) Wang, Q.; Rogers, E. T.; Gholipour, B.; Wang, C.-M.; Yuan, G.; Teng, J.; Zheludev, N. I. Optically reconfigurable metasurfaces and photonic devices based on phase change materials. *Nat. Photonics* **2016**, *10* (1), 60.
- (4) Landy, N. I.; Sajuyigbe, S.; Mock, J.; Smith, D.; Padilla, W. Perfect metamaterial absorber. *Phys. Rev. Lett.* **2008**, *100* (20), 207402.
- (5) Aydin, K.; Ferry, V. E.; Briggs, R. M.; Atwater, H. A. Broadband polarization-independent resonant light absorption using ultrathin plasmonic super absorbers. *Nat. Commun.* **2011**, *2*, 517.
- (6) Nielsen, M. G.; Pors, A.; Albrektsen, O.; Bozhevolnyi, S. I. Efficient absorption of visible radiation by gap plasmon resonators. *Opt. Express* **2012**, *20* (12), 13311–13319.
- (7) Li, W.; Guler, U.; Kinsey, N.; Naik, G. V.; Boltasseva, A.; Guan, J.; Shalae, V. M.; Kildishev, A. V. Refractory plasmonics with titanium nitride: broadband metamaterial absorber. *Adv. Mater.* **2014**, *26* (47), 7959–7965.
- (8) Liu, N.; Mesch, M.; Weiss, T.; Hentschel, M.; Giessen, H. Infrared perfect absorber and its application as plasmonic sensor. *Nano Lett.* **2010**, *10* (7), 2342–2348.

- (9) Walter, R.; Tittl, A.; Berrier, A.; Sterl, F.; Weiss, T.; Giessen, H. Large-Area Low-Cost Tunable Plasmonic Perfect Absorber in the Near Infrared by Colloidal Etching Lithography. *Adv. Opt. Mater.* **2015**, *3* (3), 398–403.
- (10) Beck, F. J.; Stavrinadis, A.; Diedenhofen, S. L.; Lasanta, T.; Konstantatos, G. Surface plasmon polariton couplers for light trapping in thin-film absorbers and their application to colloidal quantum dot optoelectronics. *ACS Photonics* **2014**, *1* (11), 1197–1205.
- (11) Li, W.; Valentine, J. Metamaterial perfect absorber based hot electron photodetection. *Nano Lett.* **2014**, *14* (6), 3510–3514.
- (12) Wu, D.; Liu, Y.; Li, R.; Chen, L.; Ma, R.; Liu, C.; Ye, H. Infrared perfect ultra-narrow band absorber as plasmonic sensor. *Nanoscale Res. Lett.* **2016**, *11* (1), 483.
- (13) Bagheri, S.; Strohfeldt, N.; Sterl, F.; Berrier, A.; Tittl, A.; Giessen, H. Large-area low-cost plasmonic perfect absorber chemical sensor fabricated by laser interference lithography. *ACS Sensors* **2016**, *1* (9), 1148–1154.
- (14) Li, L.; Hutter, T.; Finnemore, A. S.; Huang, F. M.; Baumberg, J. J.; Elliott, S. R.; Steiner, U.; Mahajan, S. Metal oxide nanoparticle mediated enhanced Raman scattering and its use in direct monitoring of interfacial chemical reactions. *Nano Lett.* **2012**, *12* (8), 4242–4246.
- (15) Baumberg, J. J.; Kelf, T. A.; Sugawara, Y.; Cintra, S.; Abdelsalam, M. E.; Bartlett, P. N.; Russell, A. E. Angle-resolved surface-enhanced Raman scattering on metallic nanostructured plasmonic crystals. *Nano Lett.* **2005**, *5* (11), 2262–2267.
- (16) Akselrod, G. M.; Ming, T.; Argyropoulos, C.; Hoang, T. B.; Lin, Y.; Ling, X.; Smith, D. R.; Kong, J.; Mikkelsen, M. H. Leveraging nanocavity harmonics for control of optical processes in 2D semiconductors. *Nano Lett.* **2015**, *15* (5), 3578–3584.
- (17) Poddubny, A. N.; Ginzburg, P.; Belov, P. A.; Zayats, A. V.; Kivshar, Y. S. Tailoring and enhancing spontaneous two-photon emission using resonant plasmonic nanostructures. *Phys. Rev. A: At, Mol, Opt. Phys.* **2012**, *86* (3), No. 033826.
- (18) Buckley, S.; Radulaski, M.; Zhang, J. L.; Petykiewicz, J.; Biermann, K.; Vučković, J. Nonlinear frequency conversion using high-quality modes in GaAs nanobeam cavities. *Opt. Lett.* **2014**, *39* (19), 5673–5676.
- (19) Zhang, N.; Zhou, P.; Cheng, D.; Weng, X.; Xie, J.; Deng, L. Dual-band absorption of mid-infrared metamaterial absorber based on distinct dielectric spacing layers. *Opt. Lett.* **2013**, *38* (7), 1125–1127.
- (20) Cetin, A. E.; Kaya, S.; Mertiri, A.; Aslan, E.; Erramilli, S.; Altug, H.; Turkmen, M. Dual-band plasmonic resonator based on Jerusalem cross-shaped nanoapertures. *Photonics and Nanostructures-Fundamentals and Applications* **2015**, *15*, 73–80.
- (21) Tuong, P.; Park, J.; Rhee, J.; Kim, K.; Jang, W.; Cheong, H.; Lee, Y. Polarization-insensitive and polarization-controlled dual-band absorption in metamaterials. *Appl. Phys. Lett.* **2013**, *102* (8), No. 081122.
- (22) Liu, X.; Tyler, T.; Starr, T.; Starr, A. F.; Jokerst, N. M.; Padilla, W. J. Taming the blackbody with infrared metamaterials as selective thermal emitters. *Phys. Rev. Lett.* **2011**, *107* (4), No. 045901.
- (23) Cetin, A. E.; Korkmaz, S.; Durmaz, H.; Aslan, E.; Kaya, S.; Paiella, R.; Turkmen, M. Quantification of Multiple Molecular Fingerprints by Dual-Resonant Perfect Absorber. *Adv. Opt. Mater.* **2016**, *4* (8), 1274–1280.
- (24) Lin, H.; Yi, Z.; Hu, J. Double resonance 1-D photonic crystal cavities for single-molecule mid-infrared photothermal spectroscopy: theory and design. *Opt. Lett.* **2012**, *37* (8), 1304–1306.
- (25) Moreau, A.; Ciraci, C.; Mock, J. J.; Hill, R. T.; Wang, Q.; Wiley, B. J.; Chilkoti, A.; Smith, D. R. Controlled-reflectance surfaces with film-coupled colloidal nanoantennas. *Nature* **2012**, *492* (7427), 86.
- (26) Bowen, P. T.; Smith, D. R. Coupled-mode theory for film-coupled plasmonic nanocubes. *Phys. Rev. B: Condens. Matter Mater. Phys.* **2014**, *90* (19), 195402.
- (27) Akselrod, G. M.; Huang, J.; Hoang, T. B.; Bowen, P. T.; Su, L.; Smith, D. R.; Mikkelsen, M. H. Large-area metasurface perfect absorbers from visible to near-infrared. *Adv. Mater.* **2015**, *27* (48), 8028–8034.
- (28) Huang, J.; Liu, C.; Zhu, Y.; Masala, S.; Alarousu, E.; Han, Y.; Fratallocchi, A. Harnessing structural darkness in the visible and infrared wavelengths for a new source of light. *Nat. Nanotechnol.* **2016**, *11* (1), 60–66.
- (29) Kinkhabwala, A.; Yu, Z.; Fan, S.; Avlasevich, Y.; Müllen, K.; Moerner, W. Large single-molecule fluorescence enhancements produced by a bowtie nanoantenna. *Nat. Photonics* **2009**, *3* (11), 654–657.
- (30) Hoang, T. B.; Akselrod, G. M.; Mikkelsen, M. H. Ultrafast room-temperature single photon emission from quantum dots coupled to plasmonic nanocavities. *Nano Lett.* **2016**, *16* (1), 270–275.
- (31) Rozin, M. J.; Rosen, D. A.; Dill, T. J.; Tao, A. R. Colloidal metasurfaces displaying near-ideal and tunable light absorbance in the infrared. *Nat. Commun.* **2015**, *6*, 7325.
- (32) Baumberg, J. J.; Aizpurua, J.; Mikkelsen, M. H.; Smith, D. R. Extreme nanophotonics from ultrathin metallic gaps. *Nat. Mater.* **2019**, *18*, 668–678.